CHAPTER 4

Cr-Zn Substituted $Sr_{1-x}Cr_xFe_{12-x}Zn_xO_{19}$ Series

4.1 Introduction

In the previous chapter, M_s of strontium hexaferrite was effectively improved but at the cost of H_c value, while improvement in H_c was attained at an almost unaffected M_s value than pristine SrM magnet. The improvement in H_c value is found to be very significant due to the substitution of Cr ion at the Fe site, almost 1.8 times. Cr ion substitution at Sr site is also reported to maintain the hard magnetic characteristic of strontium hexaferrite (Zahid et al., 2022). Accordingly, the substitution of Cr^{3+} ion at Sr^{2+} lattice site can be considered to increase the coercivity of SrM. Zn^{2+} is a non-magnetic ion ($0\mu_B$) and it is conveyed to enhance the net magnetization moment of SrM by replacing the Fe ion on $4f_1$ (↓) lattice site (Lee et al., 2005). So, a composition of $Sr_{1-x}Cr_xFe_{12-y}Zn_yO_{19}$ (x,y = 0,0; 0.2,0; 0.2,0.2; 0.4,0.4; 0.6,0.6; 0.8,0.8; 0,1) is ascertained to study the effect Cr-Zn substitution in SrM. In this chapter, the feasibility of enhancing the magnetic properties in strontium hexaferrite has been further studied.

4.2 Results and Discussion

4.2.1 Structural Properties

Fig. 4.1 shows the x-ray diffraction (XRD) patterns of auto-combustion synthesized $Sr_{1-x}Cr_xFe_{12-y}Zn_yO_{19}$ ($0 \le x \le 0.8$; $0 \le y \le 1$) calcined powder. Diffraction peaks are matched with the standard ICDD card 79-1412 and are indexed accordingly. The characteristic pattern confirms the successful formation of strontium hexaferrite with a hexagonal structure having a space group of $P6_3/mmc$. Structural parameters are given in Table 4.1.

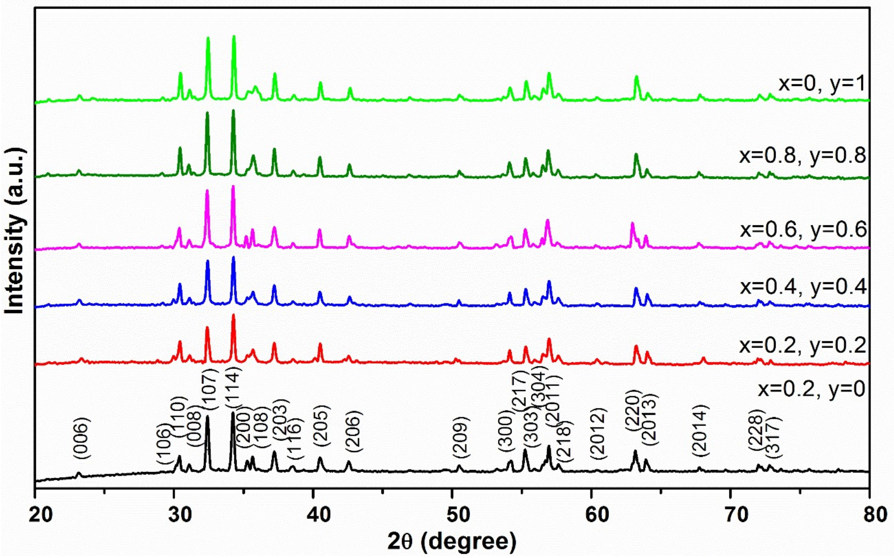

Figure 4.1 *XRD patterns of $Sr_{1-x}Cr_xFe_{12-y}Zn_yO_{19}$ ($0 \leq x \leq 0.8$; $0 \leq y \leq 1$)hexaferrites.*

Table 4.1 *Structural parameters of $Sr_{1-x}Cr_xFe_{12-y}Zn_yO_{19}$ ($0 \leq x \leq 0.8$; $0 \leq y \leq 1$) hexaferrites.*

Composition	**Lattice Parameter**		***c/a***	***V***	***D***	ϵ	χD
	***a, b* (Å)**	***c* (Å)**		**(Å^3)**	**(nm)**	**(10^{-3})**	**g/cm^3)**
x=0.2, y=0	5.88	22.99	3.91	688.37	41.16	0.0029	5.088
x=0.2, y=0.2	5.87	23.02	3.92	686.93	45.45	0.0026	5.108
x=0.4, y=0.4	5.87	22.99	3.92	686.03	46.31	0.0025	5.089
x=0.6, y=0.6	5.87	23.02	3.92	686.93	48.11	0.0024	5.057
x=0.8, y=0.8	5.87	23.00	3.92	686.33	48.47	0.0024	5.037
x=0, y=1	5.87	22.96	3.91	685.14	48.76	0.0024	5.193

The variation in lattice parameter *a* is nearly constant with the Cr-Zn content, whereas lattice parameter *c* decreases marginally. The decrease in lattice parameter *c* has resulted from the ionic radii difference (Δr) of substituted ions (Sr^{2+} = 1.13Å, Cr^{3+} = 0.63Å, Fe^{3+} = 0.67Å, Zn^{2+} = 0.74Å (Huang et al., 2015; Liu et al., 2019a). A decrease in ionic radius theoretically decreases the lattice parameter (Liu et al., 2019b). Replacement of Sr^{2+} ion by Cr^{3+} ion gives the negative ionic radius resultant (Δr = -0.50) while substitution of Zn^{2+} ion at the place of Fe^{3+} ion gives the positive ionic radius resultant (Δr = +0.07). It is not reflected in the lattice parameter variation of all the compositions. So, the other reason behind these variations might be the change in exchange-energy and the creation of oxygen vacancies to retain the charge balance (Banihashemi et al., 2021). The *c/a* ratio is used to deliberate the structure type of material, which should be lower than 3.98 for magnetoplumbite structure (Shooshtary Veisi et al., 2019). As shown in Table 4.1, the *c/a* ratio is less than 3.98, which approves the magnetoplumbite hexagonal structure formation in all samples. The average crystallite size (*D*) is observed between 41.16-48.76 nm, which confirms the formation of single-domain particles in all samples because it is lesser to a huge extent than the critical single domain size of ~500 nm for pure strontium hexaferrite driven by Kittle's theory of single domain creation (Luo et al., 2012). X-ray density is directly proportional to the molecular weight of ions and is observed to vary in the same manner.

4.2.2 Spectroscopic Properties

FT-IR spectroscopy of desiccated calcined powder of $Sr_{1-x}Cr_xFe_{12-y}Zn_yO_{19}$ ($0 \leq x \leq 0.8$; $0 \leq y \leq 1$) hexaferrites in the range of 4000-400 cm^{-1} is shown in Fig. 4.2. The spectral study gives the specific detailing of intermediate structural changes aroused due to the calcination process. In strontium hexaferrite, three characteristic peaks appear in the 400-700 cm^{-1} range. The absorption band ranges from 400-500 cm^{-1} corresponds to the intrinsic vibrations of Fe-O at octahedral sites, while the absorption band ranges between 500-700 cm^{-1} caused by the intrinsic vibrations of Fe-O at tetrahedral sites (Baniasadi et al., 2014). The difference in Fe^{3+}-O^{2-} coupling at the tetrahedral and octahedral interstices results in the variation of band positions. These bands are represented by the spring model with ν_1, ν_2 (tetrahedral), and ν_3 (octahedral) which are in accordance to Hooke's law and listed in Table 4.2 along with the bond length (r).

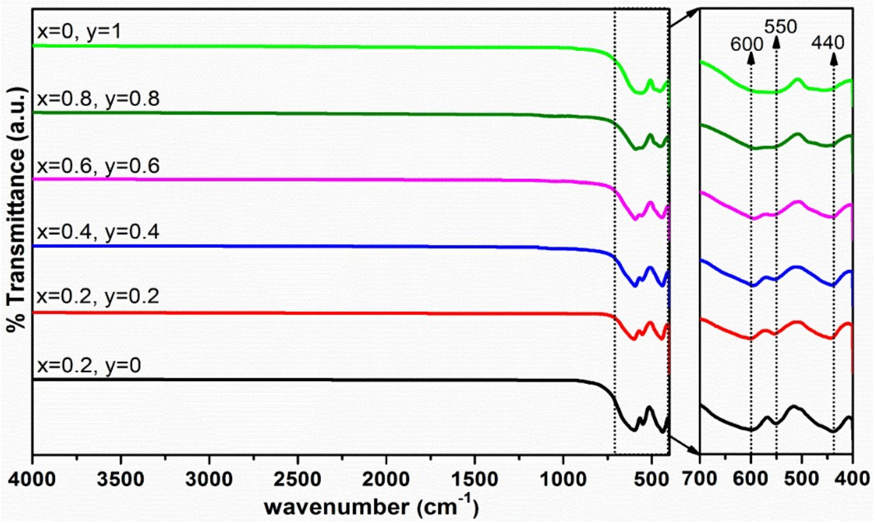

Figure 4.2 *FT-IR spectra of calcined $Sr_{1-x}Cr_xFe_{12-y}Zn_yO_{19}$ ($0 \leq x \leq 0.8$; $0 \leq y \leq 1$) hexaferrites.*

Table 4.2 *Characteristic absorption peaks [ν_1, ν_2 (tetrahedral) & ν_3 (octahedral)] and bond length (r) of $Sr_{1-x}Cr_xFe_{12-y}Zn_yO_{19}$ ($0 \leq x \leq 0.8$; $0 \leq y \leq 1$) hexaferrites.*

Composition	ν_1 (cm^{-1})	r_1 (Å)	ν_2 (cm^{-1})	r_2 (Å)	ν_3 (cm^{-1})	r_3 (Å)
x=0.2, y=0	600	4.40	550	4.66	440	5.41
x=0.2, y=0.2	600	4.40	553	4.64	443	5.38
x=0.4, y=0.4	595	4.42	554	4.64	443	5.38
x=0.6, y=0.6	593	4.43	557	4.62	440	5.41
x=0.8, y=0.8	590	4.45	-	-	445	5.37
x=0, y=1	570	4.55	-	-	455	5.29

In the samples, three characteristic peaks appear in the absorption bands ν_3 (440–455 cm^{-1}), ν_2 (550–557 cm^{-1}), and ν_1 (570–600 cm^{-1}). These are in the standard absorption band range reported for strontium hexaferrite and confirm the successful formation of an M-type hexagonal structure (Mali & Ataie, 2005). It can be observed that position of ν_2 band becomes indistinguishable due to the high content of Zn ion (y > 0.6) (Baniasadi et al., 2014). It is overlapped as a consequence of the shifted characteristic peaks of hexaferrite. The dominancy in shifting of ν_1 band suggests the occupying preference of Zn ion towards the tetrahedral site. The shifting of ν_1 band is towards lower frequencies, according to

Hooke's law, i.e., wavenumber is inversely related to the atomic weight. The characteristic resilient peaks represent the chemical polarization strengthening of internal chemical bonds due to Cr-Zn substitution and oxygen atom sharing of the Fe(Sr)-O bond. It confirms the involvement of the Cr-Zn ion in the strontium hexaferrite structure.

4.2.3 Densification and Microstructural Properties

The density of all compositions is estimated by Archimedes' methodology and listed in Table 4.3, along with the porosity. With the increasing content of substituted ions, bulk density is observed to improve with a reduction in porosity. Bulk density is lower than the x-ray density of compositions, which indicates the formation of micropores and irregular grains during the sintering process. Furthermore, EDX measurement is carried out for quantitative elemental analysis, which confirms the presence of Sr, Cr, Fe, Zn, and O elements in the respective samples. The atomic weight percentages of the elements are mentioned in Table 4.3.

Table 4.3 *Atomic weight %, average grain size (G_{avg}), bulk density (BD), and porosity (P) of $Sr_{1-x}Cr_xFe_{12-y}Zn_yO_{19}$ ($0 \le x \le 0.8$; $0 \le y \le 1$) hexaferrites.*

Composition	**Atomic weight %**					G_{avg}	***BD***	**Porosity**
	Sr	**Cr**	**Fe**	**Zn**	**O**	**(µm)**	**(g/cm³)**	**(%)**
x=0.2, y=0	6.57	0.94	63.48	-	29.01	1.36	4.55	11.13
x=0.2, y=0.2	6.54	0.93	62.31	1.19	29.03	1.97	4.59	10.18
x=0.4, y=0.4	4.93	1.91	61.54	2.33	29.29	2.07	4.61	9.38
x=0.6, y=0.6	3.26	2.89	60.73	3.67	29.45	2.12	4.78	5.38
x=0.8, y=0.8	1.61	3.92	59.98	4.94	29.55	2.33	4.78	5.03
x=0, y=1	8.09	-	57.24	6.01	28.66	2.70	4.92	4.85

Fig. 4.3 shows SEM micrograph of $Sr_{1-x}Cr_xFe_{12-y}Zn_yO_{19}$ ($0 \le x \le 0.8$; $0 \le y \le 1$) hexaferrite. These micrographs confirm the formation of hexagonal platelet-like morphology in all samples. The average grain (G_{avg}) size is listed in Table 4.3.

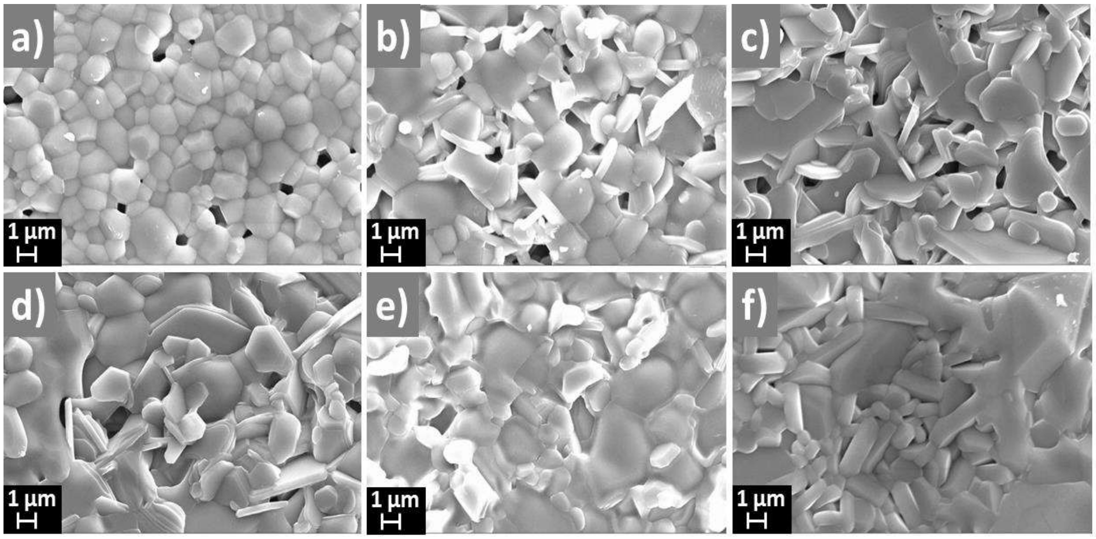

Figure 4.3 *SEM micrographs of a)* $SrCr_{0.2}Fe_{12}O_{19}$*, b)* $SrCr_{0.2}Fe_{11.8}Zn_{0.2}O_{19}$*, c)* $SrCr_{0.4}Fe_{11.6}Zn_{0.4}O_{19}$*, d)* $SrCr_{0.6}Fe_{11.4}Zn_{0.6}O_{19}$*, e)* $SrCr_{0.8}Fe_{11.2}Zn_{0.8}O_{19}$*, and f)* $SrFe_{11}ZnO_{19}$ *hexaferrites.*

Fig. 4.3 shows SEM micrograph of $Sr_{1-x}Cr_xFe_{12-y}Zn_yO_{19}$ ($0 \leq x \leq 0.8$; $0 \leq y \leq 1$) hexaferrite. These micrographs confirm the formation of hexagonal platelet-like morphology in all samples. The average grain (G_{avg}) size is listed in Table 4.3. An increasing pattern of G_{avg} is observed with the increasing content of Cr-Zn ions. The presence of a low melting Zn ion is the reason for grain growth in the samples. Zn ions have a low melting point of 420ºC (Tsao et al., 2002), which can be dissolved with high solubility in the samples resulting in grain growth. Due to the existence of remanence magnetization in a ferromagnetic material, dipole-dipole interaction occurs between particles that cause the transformation of locally released magnetic energy into heat (Abdellahi et al., 2018). This locally generated heat also promotes the formation of large agglomerates. Certain amounts of nanoparticles are diffused together, which is resulted from the Fe-Zn diffusion that promotes the self-assembly process of Fe-Zn particle growth. This effect can be explained by four sub-step of the ex-solution process, i.e., diffusion, reduction, nucleation, and growth. Fe-Zn ions diffuse together from bulk to the surface under the driving force of segregation energy which is lower on the surface than in bulk.

Due to Gibbs free energy, these ions are further reduced, nucleate, and grow into sizes where the size is dependent on the treatment time.

4.2.4 Magnetic Properties

Fig. 4.4 shows magnetic hysteresis loops of $Sr_{1-x}Cr_xFe_{12-y}Zn_yO_{19}$ ($0 \leq x \leq 0.8$; $0 \leq y \leq 1$) sintered pellets at 300 K, and different magnetic parameters are listed in Table 4.4.

Saturation magnetization (M_s) values are observed in the range of 55.4-77.9 emu/g. It is an intrinsic property of materials, which highly depends on the atomic origin of magnetism and involves quantum phenomena like exchange interaction, interatomic hopping, crystal field interaction, and spin-orbit coupling (Skomski & Sellmyer, 2008). The $Sr_{1-x}Cr_xFe_{12-y}Zn_yO_{19}$ ($0 \leq x \leq 0.8$; $0 \leq y \leq 1$) hexaferrite samples have shown an increasing pattern of M_s with the increasing content of both Cr^{3+} and Zn^{2+} ions. Substituting the non-magnetic Sr^{2+} ion with the magnetic Cr^{3+} ($3\mu_B$) ion has resulted in the increment of magnetization value. Replacing the divalent Sr^{2+} ion with trivalent Cr^{3+} ion has create the unbalanced Fe^{3+} ions distribution. It results in valance changes that causes the transformation of Fe^{3+} ions into Fe^{2+} at the *2a* (↑) or *4f₂* (↓) lattice site (Liu et al., 2019a). Transformation of more Fe^{3+} ions into Fe^{2+} at the $4f_2$ lattice site would result in the drop of the down-spin moment of Fe^{3+} ions and strengthen the magnetization of samples. The reported mössbauer study suggests that the occupying tendency of non-magnetic Zn^{2+} ions is higher towards the $4f_1$ (↓) and *2b* (↑) lattice sites (Lee et al., 2005). According to the ferrimagnetic theory, tendency of Zn^{2+} ions to occupy the $4f_1$ lattice site would increase the M_s value by increasing the net magnetic moment in the spin-up direction. The increasing value of M_s confirms the incorporation of Zn^{2+} ions at the $4f_1$ (↓) lattice site, which is the reason behind the increment of M_s value with the Zn content. The Bohr magneton number (μ_B) is observed to increase with the Zn substitution content. It is also a reason for the varying trend of M_s value.

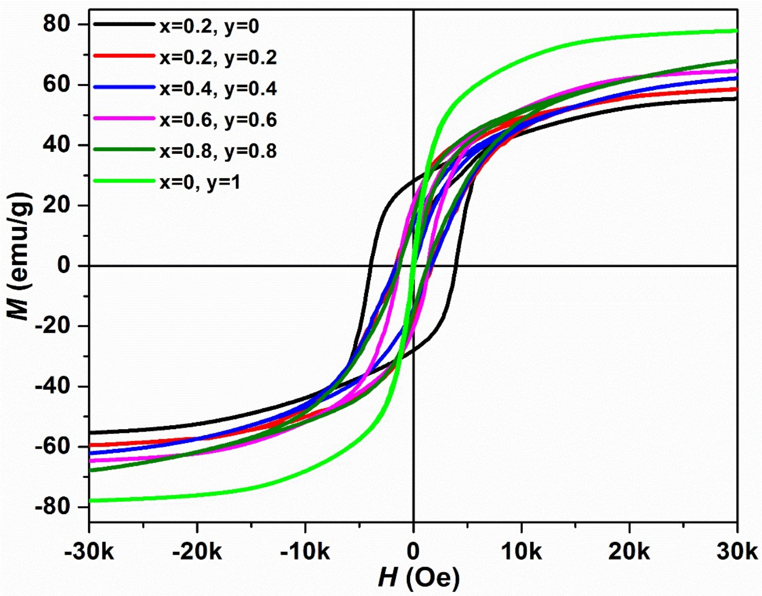

Figure 4.4 *M-H hysteresis curve of* $Sr_{1-x}Cr_xFe_{12-y}Zn_yO_{19}$ $(0 \leq x \leq 0.8;\ 0 \leq y \leq 1)$ *hexaferrites.*

Table 4.4 *Saturation magnetization* (M_s)*, remanent magnetization* (M_r)*, squareness ratio* (M_r/M_s)*, coercivity* (H_c)*, magnetocrystalline anisotropy field* (H_a)*, and effective magnetic anisotropy* (K_{eff}) *of* $Sr_{1-x}Cr_xFe_{12-y}Zn_yO_{19}$ $(0 \leq x \leq 0.8;\ 0 \leq y \leq 1)$ *hexaferrites at 300 K.*

Composition	M_s **(emu/g)**	M_r **(emu/g)**	$\frac{M_r}{M_s}$	μ_B	H_c **(Oe)**	H_a **(kOe)**	K_{eff} **(10^5 erg/g)**
$Sr_{0.8}Cr_{0.2}Fe_{12}O_{19}$	55.4	28.07	0.51	10.46	3945.7	17.84	4.94
$Sr_{0.8}Cr_{0.2}Fe_{11.8}Zn_{0.2}O_{19}$	58.5	16.55	0.28	11.07	1637.4	17.45	5.11
$Sr_{0.6}Cr_{0.4}Fe_{11.6}Zn_{0.4}O_{19}$	62.2	13.90	0.22	11.71	1599.2	16.46	5.12
$Sr_{0.4}Cr_{0.6}Fe_{11.4}Zn_{0.6}O_{19}$	64.6	20.71	0.32	12.10	1333.2	15.97	5.16
$Sr_{0.2}Cr_{0.8}Fe_{11.2}Zn_{0.8}O_{19}$	67.9	16.24	0.24	12.65	1272.2	15.46	5.25
$SrFe_{11}ZnO_{19}$	77.9	1.94	0.02	14.94	63.9	13.87	5.40

Remanent magnetization (M_r) values are observed in the range of 1.94-28.07 emu/g. It is characterized as the extrinsic magnetic property of materials that depends on the history of samples, including everything that affects the size and texture of grains (Fersi et al., 2014). Variation in the M_r value is not representing any particular behavior of substitutional elements, and its variation is random. The involvement of various synthesizing factors and grain morphology may be the reason for such variation. The area inside the hysteresis loop represents the work performed by the externally applied field to reverse the magnetization and dissipate it as heat. Commonly, dissipation in magnetic material includes magnetostriction and domain wall motion. The shape of the hysteresis loop is studied by the squareness ratio, and it proposes the behavior of magnetic domains. In the hysteresis loop, the square-like shape suggests a high degree of symmetry, while the concave-like shape suggests that wall pinning is the dominant factor that affects coercivity. The squareness ratio (M_r/M_s) is observed between 0.02-0.51. It is used as an indication of single ($M_r/M_s \geq 0.5$) and multi ($M_r/M_s < 0.5$) magnetic domain formation in the sample. Except for the $Sr_{0.8}Cr_{0.2}Fe_{12}O_{19}$, other samples have shown multi-magnetic domain formation in the samples.

Coercivity (H_c) values are observed in the range of 63.9-3945.7 Oe. The H_c value describes the remanent state stability. All sample with the Zn^{2+} ion content indicates multi-magnetic domain formation in the samples. In the multi-magnetic domain region, coercivity exhibits an inverse relationship with the particle diameter if magnetization varies due to the domain-wall motion (Kotnala & Shah, 2015). In the microstructural analysis of samples, the average grain size is found in an increasing manner with the Zn^{2+} ion content. Hence, a decreasing trend of the H_c value can be expected with the Zn content, and the same is observed within the magnetic data. Substitution of Cr^{3+} ion at the Sr lattice site is reported to maintain the hard magnetic characteristic of strontium hexaferrite (Zahid et al., 2022). The magnetocrystalline anisotropy field (H_a) of Cr substituted samples should increase with the substitutional content due to smaller ionic radii of Cr^{3+} (0.63Å) ions than the Sr^{2+} (1.13Å) ions, and high H_a will surely lead to high H_c value (Liu et al., 2019b). Hence, Cr ion is substituted at the Sr lattice site to retain the huge loss possibility of H_c value due to Zn substitution. In the $Sr_{0.8}Cr_{0.2}Fe_{12}O_{19}$ sample, single magnetic domain formation is expected to restrict the domain wall motion and demagnetization process due to the coherent spin rotation. It collectively results in a high H_c value, as observed in the $Sr_{0.8}Cr_{0.2}Fe_{12}O_{19}$ sample. In contrast, multi-magnetic domain formation facilitates domain wall motion and reduction in H_c, as observed in Zn^{2+} contained samples. A very small H_c value of the $SrFe_{11}ZnO_{19}$ sample indicates that the magnetization reversal process proceeds exclusively by domain wall motion, and it is not obstructed by any crystal imperfection (Shlyk et al., 2015).

Coercivity is also related to the magnetocrystalline anisotropy field (H_a), which sets a maximum limit of H_c that can be realized in a material. It exhibits a proportional relationship, and a similar variation trend of H_c is observed with H_a. Based on the Stoner-Wohlfarth (S-W) theory, the value of magnetocrystalline anisotropy field (H_a) and effective magnetocrystalline anisotropy (K_{eff}) are calculated by Eq. (2.14) $[K_{eff} = M_s\sqrt{(15\gamma/4)} = M_sH_a/2]$ (Almessiere et al., 2019) and given in Table 4.4. The value of γ is obtained through the slope of S-W fitting of M vs. $1/H^2$ plot as shown in Fig. 4.5.

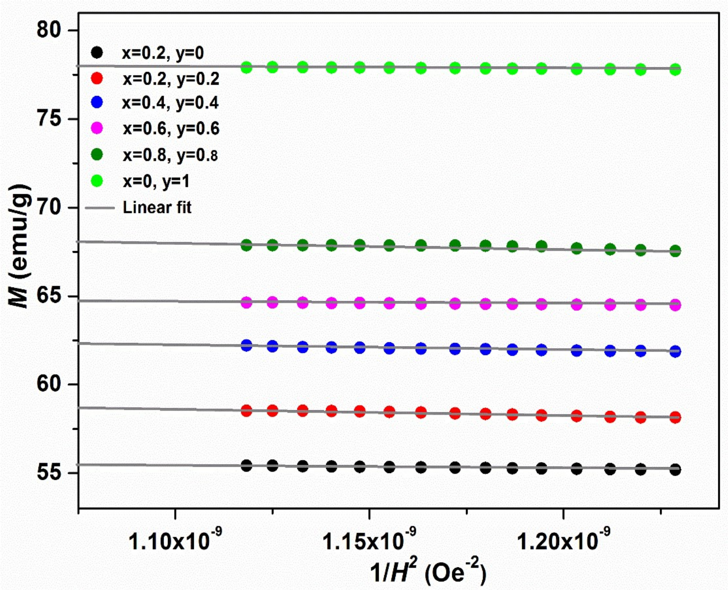

Figure 4.5 *M vs. $1/H^2$ plot with S-W linear fitting for $Sr_{1-x}Cr_xFe_{12-y}Zn_yO_{19}$ ($0 \leq x \leq 0.8$; $0 \leq y \leq 1$) hexaferrites.*

4.2.5 Dielectric Properties

Frequency-dependent characteristics of dielectric constant (ε) and dielectric tangent loss ($tan\delta$) are recorded at room temperature for $Sr_{1-x}Cr_xFe_{12-y}Zn_yO_{19}$ ($0 \leq x \leq 0.8$; $0 \leq y \leq 1$) hexaferrites and shown in Fig. 4.6 and Fig. 4.7, respectively. The values of dielectric parameters (ε, $tan\delta$) at 1 MHz frequency are listed in Table 4.5. The dielectric behavior of a material is important for design and fabrication purposes based on the particular application area. Dielectric constant (ε) shows a typical hexaferrite behavior, i.e., decrease in ε value with increasing frequency. At initial frequencies, the value of ε is high due to the contribution of Fe^{2+} ions, oxygen vacancies, and interfacial dislocation that cause the accumulation of space charges, i.e., potential well at grain boundaries (Haq & Anis-ur-Rehman, 2021). At lower frequencies, hopping of electrons could simply follow the applied field resulting in the large polarization and hence a high value of ε. With the increasing frequency, hopping of electrons could not follow the applied field due to the nonhomogeneous nature of the material and the necessity of finite time to space charge carriers for reorganizing their axes, which causes the decreasing pattern of the dielectric constant. The occurrence of only local charge polarization at higher frequencies results in the almost constant dielectric constant at these frequencies. According to the Maxwell-Wagner and Koop model, grains (conducting layer) are dominant entity in the high-frequency domain, while grain boundaries (poorly conducting layer) are dominant entity in the low-frequency domain. The microstructural analysis of samples confirms the grain growth in the material with Zn^{2+} ion content, and it is one of the reasons for decreasing trend of the dielectric constant. The strong occupying tendency of Zn^{2+} ions at $4f_1$ site reduces the Fe^{2+} ion concentration at the tetrahedral site and hence reduces the space charge polarization in the material. It causes the reduction of ε with the increasing Zn^{2+} ion content. Moreover, Cr^{3+} ions in the samples may decrease the dielectric constant as they do not participate in the conduction mechanism however inhibits the motion of charge carriers (Rao et al., 1981).

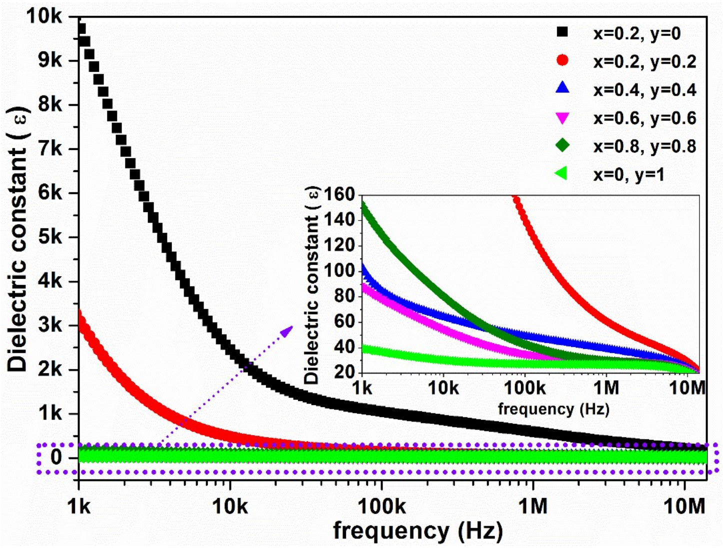

Figure 4.6 *Dielectric constant (ε) of* $Sr_{1-x}Cr_xFe_{12-y}Zn_yO_{19}$ *(*$0 \leq x \leq 0.8$*;* $0 \leq y \leq 1$*) hexaferrites with respect to frequency at room-temperature.*

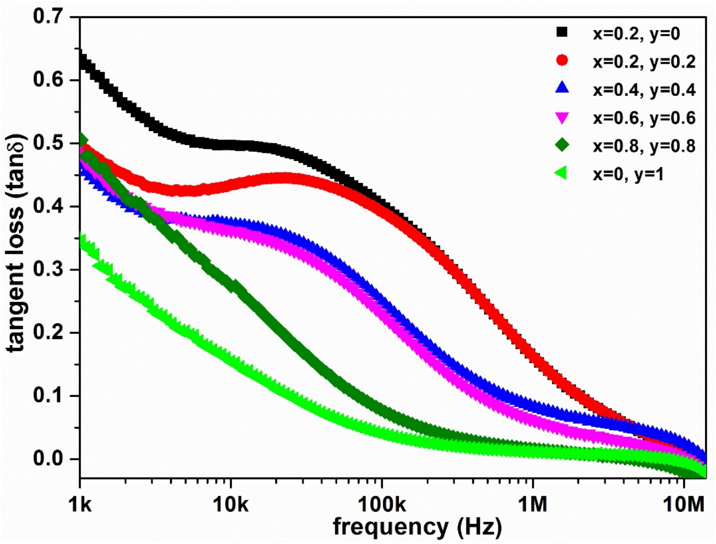

Figure 4.7 *Dielectric loss (tanδ) of* $Sr_{1-x}Cr_xFe_{12-y}Zn_yO_{19}$ *(*$0 \leq x \leq 0.8$*;* $0 \leq y \leq 1$*) hexaferrites with respect to frequency at room-temperature.*

Dielectric loss in hexaferrite materials originates from the electron hopping phenomenon in lower frequency region and from the polaron hopping phenomenon in higher frequency region (Haq & Anis-ur-Rehman, 2021). Also, the state of Fe ions in the presence of applied field, charge dipole defects, and their state-changing response contributes to the dielectric loss. Dielectric tangent loss is observed to decrease with the Cr-Zn content. Due to increasing Zn ion content, the reduction in Fe^{2+} concentration (responsible for conduction losses) may be the reason for such variation. The value of $\tan\delta$ is observed to be small in comparison to the reported value (Asghar & Anis-Ur-Rehman, 2012), which makes the samples very appropriate for high-frequency applications.

Table 4.5 *Room-temperature value of dielectric constant (ε), tangent loss ($\tan\delta$), resistivity (ρ) and conductivity (σ) of $Sr_{1-x}Cr_xFe_{12-y}Zn_yO_{19}$ ($0 \leq x \leq 0.8$; $0 \leq y \leq 1$) hexaferrites at 1MHz frequency.*

Composition	ε	$\tan\delta$	ρ (10^6 Ω-cm)	σ (10^{-7} S-cm^{-1})
x=0.2, y=0	591.1	0.159	1.9	526.3
x=0.2, y=0.2	60.5	0.161	18.1	55.2
x=0.4, y=0.4	38.9	0.082	54.8	18.2
x=0.6, y=0.6	30.4	0.061	94.4	10.6
x=0.8, y=0.8	29.6	0.016	374.5	2.7
x=0, y=1	26.7	0.011	578.2	1.7

4.2.6 Electrical Properties

Electrical properties give insight into the conduction mechanism. The frequency-dependent characteristic of resistivity (ρ) at room-temperature is shown in Fig. 4.8. The values of resistivity and conductivity at the 1 MHz frequency are listed in Table 4.5.

One unit cell of strontium hexaferrite contains two divalent Sr^{2+} cations, twenty-four trivalent Fe^{3+} cations, and thirty-eight divalent O^{2-} anions. The synthesis (by any process) of hexaferrite materials requires post-synthesis heat treatment at elevated temperatures for phase purity. During this heat treatment process, some O^{2-} ions are expected to loss. For charge neutrality, some Fe^{3+} ions are changed to Fe^{2+} ions but do not rechange to Fe^{3+} as they cannot be oxidized further in grain during cooling (Asghar & Anis-

Ur-Rehman, 2012). The presence of Fe^{2+} ions is the charge carrier source and the reason behind the conduction mechanism in ferrites. In M-type hexaferrite materials, electron hopping between Fe^{2+} and Fe^{3+} ions present at octahedral sites are mainly responsible for the electrical conduction mechanism, according to Verwey model. The hopping probability is influenced by activation energy and the separation between the involved ions (Lakshman et al., 2005). The hopping mechanism between the octahedral-octahedral sites has the highest probability due to smaller metal ions distance. The incorporation of Zn^{2+} ions in SrM structure replaces Fe^{3+} ions from the tetrahedral site. In order to maintain the charge neutrality, Fe^{2+} ions at the octahedral site are transformed to Fe^{3+} and hence decrease the Fe^{2+} concentration at this site. It lessens the concentration of charge carriers accountable for the electrical conduction and results in the higher resistivity of the material.

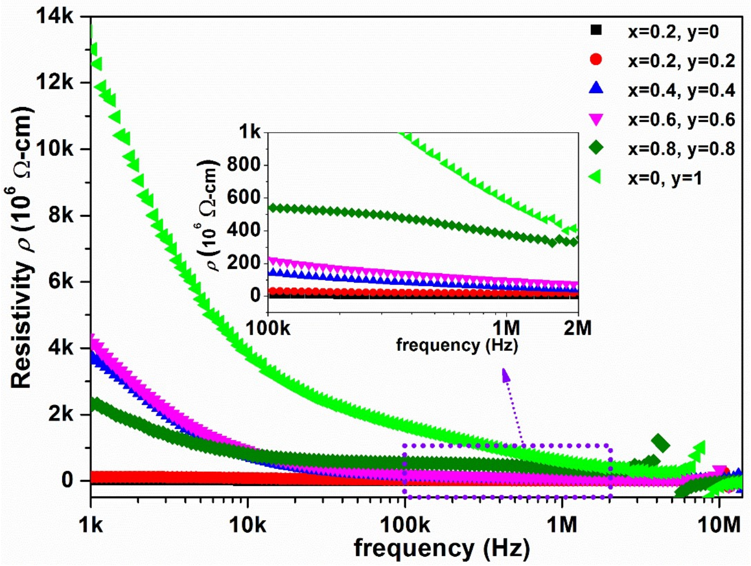

Figure 4.8 *Frequency-dependent resistivity variation in* $Sr_{1-x}Cr_xFe_{12-y}Zn_yO_{19}$ *(*$0 \leq x \leq 0.8$*;* $0 \leq y \leq 1$*) hexaferrite.*

4.3 Conclusions

A composition of $Sr_{1-x}Cr_xFe_{12-y}Zn_yO_{19}$ ($0 \leq x \leq 0.8$; $0 \leq y \leq 1$) was effectively synthesized by the self-propagating sol-gel auto-combustion process. The structural studies confirm the formation of a hexagonal structure with the *P6₃/mmc* space group. The substitution of Zn ion is found to be responsible for the densification and grain growth in the sample. Magnetic studies suggest the improvement of H_c with the Cr^{3+} ion substitution at Sr site, and it is also observed to suppress the dilution of H_c value towards the soft magnet. Despite the sharp H_c dilution due to Zn^{2+} ion, Cr^{3+} substitution maintained the hard magnetic characteristic of samples because the observed H_c values in Cr^{3+} contained samples are still greater than 1 kOe. Substitution of Zn^{2+} ion enhanced the M_s value, even higher than the maximum theoretical M_s value of SrM (~72 emu/g). A high value of M_s ~78 emu/g is observed for the $SrFe_{11}ZnO_{19}$ composition with an extreme dilution in H_c value ~63.9 Oe, which changes the hard magnetic characteristic of strontium hexaferrites towards the soft magnetic characteristic.